A vegetation phenology dataset by integrating multiple sources using the Reliability Ensemble Averaging method

Yishuo Cui [1], Shouzhi Chen[1], Yufeng Gong[1], Mingwei Li[1], Zitong Jia[1], Yuyu Zhou[2], Yongshuo H. Fu[1,3]

[1]College of Water Sciences, Beijing Normal University, Beijing 100875, China
5 [2]Department of Geography, The University of Hong Kong, Hong Kong, China
[3]Plants and Ecosystems, Department of Biology, University of Antwerp, Antwerp, Belgium

Correspondence to: Yongshuo H. Fu (yfu@bnu.edu.cn), Yuyu Zhou (yuyuzhou@hku.hk)

Abstract. Global change has substantially shifted vegetation phenology, with important implications in the carbon and water cycles of terrestrial ecosystems. Various vegetation phenology datasets have been developed using remote sensing data;
10 however, the significant uncertainties in these datasets limit our understanding of ecosystem dynamics in terms of phenology. It is therefore crucial to generate a reliable large-scale vegetation phenology dataset, by fusing various existing vegetation phenology datasets, to provide comprehensive and accurate estimation of vegetation phenology with fine spatiotemporal resolution. In this study, we merged four widely used vegetation phenology datasets to generate a new dataset using the Reliability Ensemble Averaging fusion method. The spatial resolution of the new dataset is 0.05° and its temporal scale spans
15 1982–2022. The evaluation using the ground-based PhenoCam dataset from 280 sites indicated that the accuracy of the newly merged dataset was improved substantially. The start of growing season and the end of growing season in the newly merged dataset had the largest correlation (0.84 and 0.71, respectively) and accuracy in terms of the root mean square error (12 and 17 d, respectively). Using the new dataset, we found that the start of growing season exhibits a significant ($p < 0.01$) advanced trend with a rate of approximately 0.24 d yr^{-1}, and that the end of growing season exhibits a significant ($p < 0.01$) delayed
20 trend with a rate of 0.16 d yr^{-1} over the period 1982–2022. This dataset offers a unique and novel source of vegetation phenology data for global ecology studies.

1 Introduction

Global change has notably altered the timing of vegetation phenology (Ettinger et al., 2020; Zhang et al., 2022), leading to important implications in the carbon and water cycles of terrestrial ecosystems (Peñuelas et al., 2009; Piao et al., 2019;

25 Richardson et al., 2012; Zhou, 2022). Various vegetation phenology datasets using remote sensing data have been produced, but inconsistencies and uncertainties arise when comparing those datasets with ground-based phenological observations, and large variations also exist in terms of the spatiotemporal resolutions (Peng et al., 2017). Therefore, there is an urgent need to develop a highly reliable vegetation phenology product to improve our understanding of vegetation phenology dynamics, and to facilitate subsequent research on terrestrial ecosystem responses to climate change.

30 Ground-based phenological records were commonly used in vegetation phenology studies (Fu et al., 2014; Geng et al., 2020; Sparks and Carey, 1995; Zhou et al., 2020). Although ground-based observations provide high accuracy in terms of phenology dynamics, they are limited to certain locations resulting in sparse spatial coverage. In contrast, phenology datasets based on remote sensing data can cover large areas, providing comprehensive and continuous monitoring of vegetation phenology across landscapes, regions, or even continents. Additionally, remote sensing datasets are processed using

35 standardized methods that ensure consistency and comparability across different locations and periods. However, phenology datasets based on remote sensing data do have certain limitations. Owing to differences in revisit cycles among satellites, together with sensor characteristics, sun–sensor geometry, and atmospheric conditions during imaging, substantial bias exists among the derived phenology datasets. For example, differences of >50 d in the start of growing season (SOS) have been reported among different phenology datasets based on remote sensing data (Peng et al., 2017; Zhou et al., 2020). Additionally,

40 substantial variations in the trends of vegetation phenology exist. For example, a recent study reported that the SOS was delayed by 0.17 d yr^{-1} when based on the Global Inventory Modeling and Mapping Studies-3rd Generation (GIMMS 3g) dataset, whereas the SOS was advanced by 0.58 d yr^{-1} when based on the Moderate Resolution Imaging Spectroradiometer (MODIS) dataset in the Northern Hemisphere (Zhang et al., 2020). Previous studies found that different vegetation phenology datasets have merits and demerits in different regions and over different periods (Fensholt and Proud, 2012; Zhang et al., 2020).

45 Because it is difficult to determine the optimal dataset from the various phenology datasets, producing a merged dataset is therefore essential for providing a comprehensive and accurate estimation of vegetation phenology with high spatiotemporal resolution.

The simple averaging method was commonly employed when integrating different vegetation phenology datasets (Delbart et al., 2015; Piao et al., 2019; Wang et al., 2019). However, the simple averaging method operates under the

50 assumption that the reliability within each dataset is uniform, whereas it varies because of differences among the various methods of extraction (Lu et al., 2021). Alternatively, methods such as weighted functions, the Bayesian approach, and mixed models have been combined with the vegetation index method to integrate datasets with high temporal and spatial resolutions

(Walker et al., 2012; Zhu et al., 2010). Such methods can improve the data reliability of homogeneous surfaces based on the continuity of data in both time and space. Specifically, the Reliability Ensemble Averaging (REA) method, which assigns different weights to each dataset based on their reliability, has been applied to merge various datasets and consistently demonstrated high reliability through validation (Giorgi and Mearns, 2002; Lu et al., 2021; Xu et al., 2010). Therefore, the REA method has demonstrated its effectiveness in obtaining accurate merged vegetation phenology datasets.

In this study, we merged four widely used vegetation phenology datasets to generate a new dataset using the REA fusion method. The spatial resolution of the new dataset is 0.05° and its temporal scale spans 1982–2022. The new dataset was evaluated using data from the ground-based PhenoCam dataset from 280 sites over the period 2000–2018, which provided 1410 site–year combinations. We further explored the phenological trends in spring and autumn vegetation phenology using the merged dataset. The new vegetation phenology dataset could be used in further studies on the impact of energy and carbon–water cycles within terrestrial ecosystems, together with analysis of their responses and feedbacks to global climate change (Piao et al., 2009, 2019; Tang et al., 2016).

2 Data and Method

2.1 Phenology dataset

Four satellite-based vegetation phenology products were used to create a merged dataset, and the ground-based PhenoCam dataset was used for validation. The four satellite-based vegetation phenology products include (1) the MCD12Q2 dataset, which was extracted from the MODIS Land Cover Dynamics Version 6.1 derived by Friedl et al., 2022; (2) the VIP dataset (Making Earth System Data Records for Use in Research Environments Vegetation Index and Phenology), that was derived by Didan and Barreto, 2016, (3) the GIM_3g (GIMMS NDVI3g) dataset, that was derived by Wang et al. (2019), and (4) the GIM_4g (GIMMS NDVI4g) derived by Chen and Fu, 2024. The time span and the spatial resolution of each vegetation phenology dataset are listed in Table 1. The details of each phenology dataset are introduced below.

Table 1 List of data sources

Name	Abbreviations	Sensor	Spatial Resolution	Time Span	Reference
MODIS MCD12Q2	MCD12Q2	MODIS	500m	2001-2022	(Friedl et al., 2022)
MEaSUREs VIPPHEN	VIP	AVHRR& MODIS	0.05°	1982-2015	(Didan and Barreto, 2016)
GIMMS NDVI3g	GIM_3g	AVHRR	1/12°	1998-2014	(Wang et al., 2019)
GIMMS NDVI4g	GIM_4g	AVHRR	1/12°	1982-2020	(Chen and Fu, 2024)

Note: GIM_4g refers to the phenology dataset derived the from GIMMS NDVI4g dataset, MCD12Q2 refers to the MODIS MCD12Q2 product, VIP refers to the MEaSUREs VIPPHEN dataset, and GIM_3g refers to the phenology dataset derived from the GIMMS NDVI3g dataset.

2.1.1 MCD12Q2 phenology dataset

The MCD12Q2 product was derived using data from the MODIS sensor onboard the Terra and Aqua satellites. The MCD12Q2 land cover dynamic product v6.1 provides a global surface phenology dataset with a 500-m spatial resolution for the period 2001–2021. The vegetation phenology data were extracted from the Nadir Bidirectional Adjusted Reflectance 2-band Enhanced Vegetation Index (EVI2) using the threshold method (Gray et al., 2019). The MCD12Q2 phenology dataset includes greenup and dormancy (equivalent to SOS and EOS in this study, respectively). Greenup (dormancy) is defined as the date when the EVI2 time series first (last) crosses 15% of the segment EVI2 amplitude (Gray et al., 2019). This dataset can be found at https://lpdaac.usgs.gov/products/mcd12q2v061/ (Friedl et al., 2022).

2.1.2 VIP phenology dataset

The VIP phenology dataset (VIP) was generated using data from the NASA Making Earth System Data Records for Use in Research Environments (MEaSUREs) and the Advanced Very High-Resolution Radiometer (AVHRR) over the period 1981–1999, together with MODIS/Terra MOD09 surface reflectance data over the period 2000–2014 (Didan et al., 2018). The VIP dataset includes the SOS and EOS, which were also extracted using the threshold method. This dataset is organized in a geographic gridded format with a spatial resolution of 0.05°. This dataset can be found at https://lpdaac.usgs.gov/products/vipphen_ndviv004/ (Didan and Barreto, 2016).

2.1.3 GIM_3g phenology dataset

The GIMMS NDVI 3g-based phenology dataset (GIM_3g) has a spatial resolution of 1/12° and covers the period 1998–2014 (Wang et al., 2019). A double logistic function was applied to fit the NDVI curve and the threshold method was used to extract phenological dates, including the SOS and EOS. This product provides phenology data for the Northern Hemisphere, and it uses the date when the NDVI first (last) crosses 20% of the segment NDVI amplitude as the SOS (EOS). This dataset can be accessed at http://data.globalecology.unh.edu/data/GIMMS_NDVI3g_Phenology/ (Wang et al., 2019).

2.1.4 GIM_4g phenology dataset

The GIM_4g dataset, based on the GIMMS NDVI 4g dataset acquired by the AVHRR sensors, has a spatial resolution of 1/12° and a temporal scale spanning 1982–2020. Two steps were adopted in the process to extract phenological dates. First, the NDVI time series data were fitted and smoothed using five fitting methods: the HANTS-Maximum, Spline-Midpoint, Gaussian-Midpoint, Timesat-SG, and Polyfit-Maximum methods. Second, the threshold method was used to extract phenological dates, using the date when the NDVI first (last) crosses 20% (50%) of the segment NDVI amplitude as the SOS (EOS) (Chen et al., 2024; Fu et al., 2023). The average spring (SOS) and autumn (EOS) phenological dates were produced from the results of the five fitting methods. The GIM_4g phenology dataset is available at https://doi.org/10.5281/zenodo.11136967 (Chen and Fu, 2024).

2.1.5 Camera-based phenology dataset

The ground-based PhenoCam dataset, with phenological dates extracted from camera-derived images with high spatial resolution and reliable accuracy, was used to validate the merged dataset. The PhenoCam dataset comprises three datasets. The first dataset, i.e., the PhenoCam Dataset v 2.0, includes data acquired using a downward-facing automatic digital fisheye camera system over the period 2000–2018 and across 393 sites in various ecosystems, comprising deciduous broadleaf, deciduous needleleaf, evergreen broadleaf, evergreen needleleaf, grassland, mixed vegetation, shrubland, tundra, and wetland ecosystems, mainly in regions of Europe and North America (https://daac.ornl.gov/) (Moon et al., 2021; Ruan et al., 2023). The second PhenoCam dataset is the Japan Internet Nature Information System digital camera data acquired over the period 2002–2009 (Ide and Oguma, 2010; Inoue et al., 2014), and the vegetation types include deciduous broadleaf forest, wetland, and mixed deciduous forest (http://www.sizenken.biodic.go.jp/). The third dataset is from the Phenological Eyes Network (http://www.pheno-eye.org/), which is a network of ground-based observatories for long-term automatic observation of vegetation dynamics established in 2003. For use in this study, we selected PhenoCam data from 280 sites over the period 2000–2018, which provided 1410 site–year combinations.

2.1.6 Land cover dataset

To avoid the impact of human activities and non-vegetated areas on data quality, areas of cropland, cropland/natural vegetation mosaics, permanent snow and ice, barren land and water bodies were removed based on a land cover dataset obtained by supervised classification of MODIS reflectance data (Sulla-Menashe and Friedl, 2018). The land cover data generated based on the Annual International Geosphere–Biosphere Programme classification schemes, are available from https://lpdaac.usgs.gov/products/mcd12q1v061/ (Friedl and Sulla-Menashe, 2022).

2.2 Ensemble method for estimating phenological dates

The weighting method was applied to obtain more accurate SOS and EOS dates from the four vegetation phenology datasets. The weight assigned to each product was based on the interannual variability of each phenology dataset, together with the degree of consistency and offset among the four phenology datasets (Giorgi and Mearns, 2002). There is discrepancy in the spatial coverage among the four phenology datasets, and missing data occurs in specific regions for some of the datasets. The ensemble method can fill in missing data accurately, thereby producing a phenology dataset with high accuracy and spatially continuous coverage. Furthermore, the process of merging the phenology datasets does not depend on simple averaging; instead, it is based on the uncertainty among the products, which produces data that is more reliable than those obtained using the simple averaging method, and can circumvent the effects of outliers (Giorgi and Mearns, 2002).

2.2.1 Reliability ensemble averaging method

The REA method based on the "voting principle" generates data that is consistent with most of the input phenology products at the pixel level. It provides a dataset with high reliability by relying on the temporal consistency of each pixel

among the input products, and by minimizing the influence of outliers during the merging process (Giorgi and Mearns, 2002).
140   The REA method has been applied to generate datasets for multiple elemental fields, e.g., temperature, evapotranspiration, and precipitation (Giorgi and Mearns, 2002; Lu et al., 2021; Xu et al., 2010). In this study, the REA method was used to integrate both the SOS and the EOS from the four phenology datasets.

The REA method gives different weights to the various datasets involved in the process of data merging, and then obtains the desired result using the following function:

$$\widehat{\Delta Phe} = \tilde{A}(\Delta Phe) = \frac{\sum_i R_i \Delta Phe_i}{\sum_i R_i} \tag{1}$$

where $\widehat{\Delta Phe}$ represents the phenology result, ΔPhe_i represents the different datasets involved in the process, $\tilde{A}$ denotes the REA process, and R_i represents the model reliability factor, which is defined as follows:

$$R_i = \left[(R_{B,i})^m \times (R_{D,i})^n\right]^{\left[\frac{1}{m \times n}\right]}$$
$$= \left\{\left[\frac{\epsilon_{Phe}}{abs(B_{Phe,i})}\right]^m \left[\frac{\epsilon_{Phe}}{abs(D_{Phe,i})}\right]^n\right\} \tag{2}$$

where $R_{B,i}$ measures the bias of the data compared with that of the average data (the higher the bias, the lower the
150   reliability of the dataset), and $R_{D,i}$ represents the convergence criterion of the data (the larger the distance between the dataset and the newly generated REA data, the poorer the convergence; several iterations are required to reach convergence). The values of $R_{B,i}$ and $R_{D,i}$ will be set to 1 when $B_{Phe,i}$ and $D_{Phe,i}$ are less than ϵ_{Phe}, which means the deviation of the dataset is within the limit of natural variation.

$$B_{Phe,i} = \Delta Phe_i - \overline{Phe}, \tag{3}$$

155   $$D_{Phe,i} = \Delta Phe_i - \Delta Phe, \tag{4}$$

$$\varepsilon_{Phe} = \max(MA(D_{Phe})) - \min(MA(D_{Phe})). \tag{5}$$

Equation (3) explains the derivation of $B_{Phe,i}$ i.e., it is defined by the difference between the input dataset and the mean value of the four datasets. Equation (4) explains the arithmetic process of $D_{Phe,i}$, which is measured by the difference between the REA result and each input dataset. In Eq. (5), ε_{Phe} is measured by the natural variability in phenology, which is calculated
160   by estimating the difference between the maximum and minimum values of the multiyear moving averages following linear detrending of the observed long-term series data.

$$\delta_{Phe} = \left[\tilde{A}(\Delta Phe_i - \widehat{\Delta Phe})^2\right]^{\frac{1}{2}} = \left[\frac{\sum_i R_i(\Delta Phe_i - \widehat{\Delta Phe})^2}{\sum_i R_i}\right]^{\frac{1}{2}} \tag{6}$$

$$\Delta Phe_+ = \widehat{\Delta Phe} + \tilde{\delta}_{\Delta Phe}, \tag{7a}$$

$$\Delta Phe_- = \widehat{\Delta Phe} - \tilde{\delta}_{\Delta Phe}. \tag{7b}$$

165   In Eq. (6), δ_{Phe} is the uncertainty range calculated using R_i and the difference between the REA result and the datasets (a higher value of δ_{Phe} means larger differences between the REA result and the original phenology datasets). The upper and lower limits of the uncertainty range are measured by $\widehat{\Delta Phe}$ and $\tilde{\delta}_{\Delta Phe}$, respectively, in Eqs. (7a) and (7b).

2.2.3 Evaluation criteria

In this study, the metrics of the root mean square error (RMSE), BIAS, correlation coefficient (r), unbiased RMSE
170 (UbRMSE) and coefficient of variation (CV) were used for data evaluation:

$$RMSE = \sqrt{\frac{\sum_{i=1}^{n}(Phe_i - Ref_i)^2}{n}},\tag{8}$$

$$BIAS = \frac{\sum_{i=1}^{n}(Phe_i - Ref_i)}{n},\tag{9}$$

$$r = \frac{\sum_{i=1}^{n}(Phe_i - \overline{Phe})(Ref_i - \overline{Ref})}{\sqrt{\sum_{i=1}^{n}(Phe_i - \overline{Phe})^2}\sqrt{\sum_{i=1}^{n}(Ref_i - \overline{Ref})^2}},\tag{10}$$

$$ubRMSE = \sqrt{RMSE^2 - BIAS^2},\tag{11}$$

$$STD = \sqrt{\frac{1}{N}\sum_{i=1}^{N}(Phe_i - \overline{Phe})^2},\tag{12}$$

$$CV = \frac{\sigma_{Phe}}{\overline{Phe}}\tag{13}$$

where n represents the number of site years, Phe_i represents the corresponding vegetation phenological indicator (i.e.,
SOS and EOS) at a given point, Ref_i represents data from a phenology camera, σ_{Phe} represents the standard deviation of
Phe_i, and $\overline{Phe}$ and $\overline{Ref}$ represent the average of Phe_i and Ref_i, respectively.

180 **2.2.4 Mann–Kendall trend test**

The Mann–Kendall trend test is a nonparametric trend test method, which has the characteristics of not being limited by
a specific distribution and a small number of outliers, and can be used to detect the hypothesis trend of time series data (Kendall,
1975; Mao et al., 2022; Sun et al., 2019). The basic Mann–Kendall test formulas are as follows:

$$S = \sum_{i=1}^{n-1}\sum_{j=j+1}^{n} \text{sgn}(X_j - X_i),\tag{14}$$

$$Z_c = \begin{cases} \dfrac{S-1}{\sqrt{Var(S)}} & S > 0 \\ 0 & S = 0 \\ \dfrac{S+1}{\sqrt{Var(S)}} & S < 0 \end{cases}\tag{15}$$

where X_i and X_j are the phenological parameter values of the i-th year and the j-th year of the pixel, respectively, n is
the length of the time series, sgn is the sign function, and S is the test statistic. The null hypothesis H_0: the time series data is
n independent samples with identically distributed random variables, H_1: for any $i, j \leq n$, and $i \neq j$, the distribution of X_i,

X_k is different. If $|Z| \geq Z_{1-\frac{\alpha}{2}}$, the time series is considered to have a statistically significant change; otherwise, any change is

190   considered not statistically significant. When Z > 0, the time series has an upward trend; when Z < 0, it has a downward trend
(Zhou and Liu, 2018).

3 Results

3.1 Difference in vegetation phenological dates among the four datasets

Figure 1 illustrates the spatial distribution of the multiyear mean dates for both the SOS and the EOS above 30°N for each

195   of the four datasets. The mean SOS values for the MCD12Q2, VIP, GIM_3g, and GIM_4g datasets are day of the year (DOY)
120 (std = 32 d), 125 (std = 43 d), 132 (std = 17 d), and 139 (std = 32 d), respectively. Discrepancies among the datasets are
particularly notable in southwestern North America, North Africa, the Qinghai–Tibet Plateau, and Mongolia. Compared with
the SOS, the EOS exhibits greater variability, and the mean EOS values for the MCD12Q2, VIP, GIM_3g, and GIM_4g datasets
are DOY 281 (std = 37 d), 290 (std = 44 d), 315 (std = 19 d), and 287 (std = 53 d), respectively. Among the four datasets, the

200   spatial distributions of the GIM_4g and VIP datasets are the most similar. In comparison with these two datasets, the MCD12Q2
dataset displays lower EOS values in Northern Europe, Central Asia, North America, and in the 45°–60°N latitudinal belt over
Central Asia. Given the substantial differences among these datasets, it is imperative to integrate these datasets into a merged
dataset with higher accuracy.
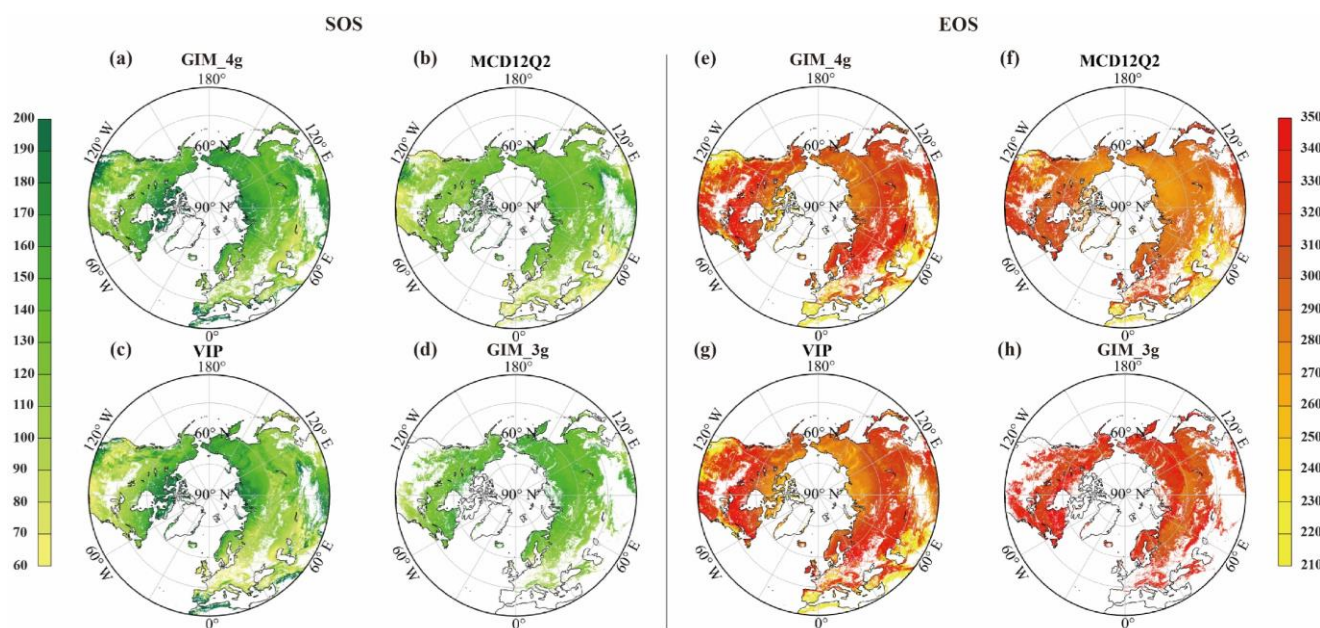
205   **Figure 1: Spatial distribution of multiyear mean SOS and EOS dates from each phenology dataset:** (a–d) multiyear mean SOS dates
and (e–h) multiyear mean EOS dates derived from the GIM_4g, MCD12Q2, VIP, and GIM_3g datasets, respectively.

3.2 Variation of weights and contributions of the four datasets to the merged phenology dataset

The weight of each dataset, as determined by the REA method, varies largely among years and specific locations. The left panels of Fig. 2 illustrate the mean weight for each dataset in each year over the period 1982–2022, with the upper and lower sections representing the SOS and the EOS, respectively. For the SOS, the overall weight of the VIP dataset during 1982–1998 surpasses that of the GIM_4g dataset. The GIM_3g dataset is dominant during 1999–2014, with weights exceeding 65%. In 2015, the weighting of the MCD12Q2 dataset was highest at approximately 45%, with the weights of the other two datasets broadly similar. During 2016–2020, the weights of the MCD12Q2 and GIM_4g datasets are 61% and 39%, respectively, but during 2021–2022, the dataset consists solely of the MCD12Q2 dataset. The combinations of data sources for the EOS data are similar to those for the SOS data. Specifically, during 1982–1998, the weight of the VIP dataset is approximately 65%, with the GIM_4g dataset accounting for the remaining 35%. For 1999–2000, the weighting of the GIM_3g dataset is approximately only 10%, whereas that of the VIP dataset is the highest (approximately 55%). Throughout the period 2001–2014, the weighting of the VIP dataset is greatest (>45%), whereas that of the GIM_3g dataset is low (<10%); the weighting of the GIM_4g and MCD12Q2 datasets each account for over 20%. During 2016–2020, the weights of the GIM_4g and MCD12Q2 datasets are broadly equal, albeit with the weighting of the GIM_4g dataset slightly exceeding that of the MCD12Q2 dataset.

The latitudinal distribution of the mean weighting of the datasets for the SOS and the EOS is shown in Fig. 2(b) and 2(d), respectively. For the SOS data, the zonal distribution of the GIM_4g, VIP, and MCD12Q2 datasets is reasonably stable within 30°–75°N. The weight of the GIM_3g dataset is notably higher between 50°N and 70°N, primarily because of its spatial distribution, and it shows notable fluctuations in high-latitude areas. In contrast, the weighting of the EOS datasets exhibits relatively smooth changes within 30°–75°N. There are marked fluctuations in the weighting of the GIM_4g and VIP datasets in high-latitude areas above 75°N. The weight of the GIM_4g dataset between 30°N and 75°N fluctuates before stabilizing smoothly. Conversely, the weight of the VIP dataset increases with latitude, displaying a trend opposite to that of the GIM_4g dataset. Additionally, the weighting of both the MCD12Q2 and the GIM_3g datasets initially increases and then decreases with increasing latitude.
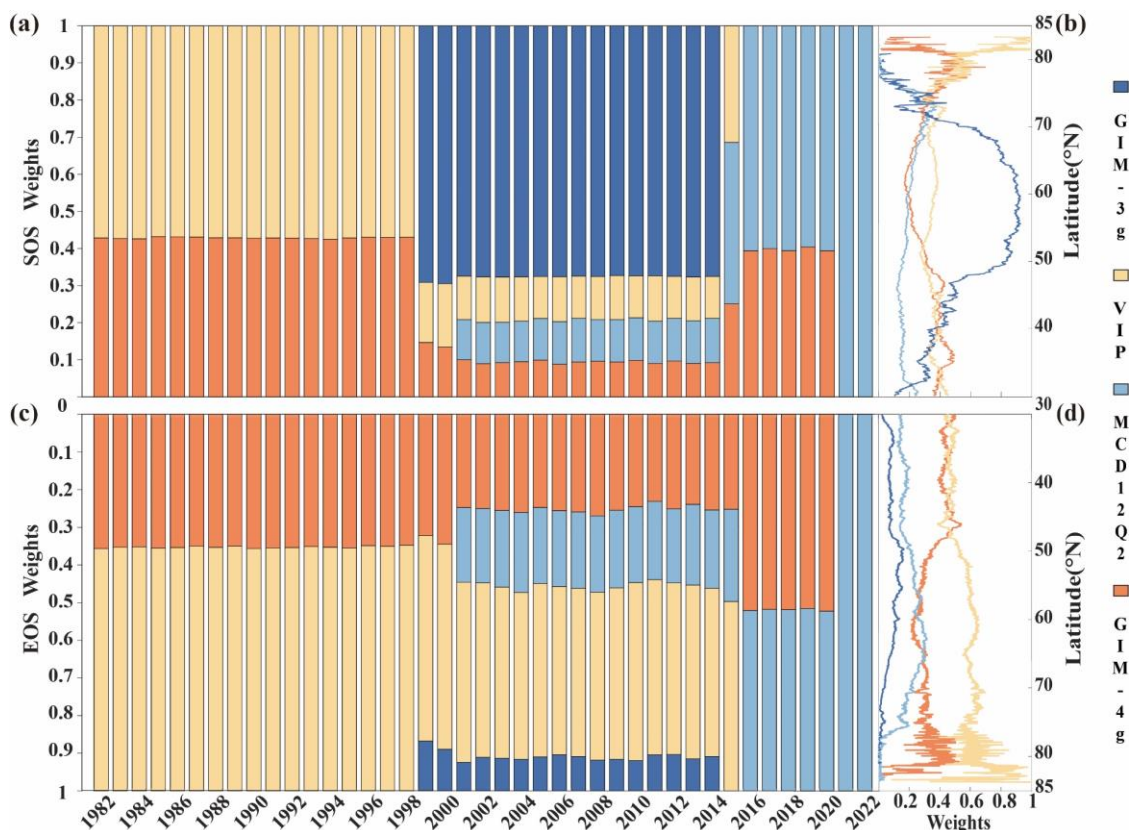
Figure 2: (a and c) Weights of the four phenology datasets during 1982–2022 and (b and d) latitudinal differences for (a and b) the SOS and (c and d) the EOS. The four datasets comprise the GIM_4g, MCD12Q2, VIP, and GIM_3g datasets (for the full names, see Table 1).

Figure 3 shows the spatial distribution of the mean contribution of the four datasets to the merged SOS and EOS results, calculated as the average weight for each pixel over the timespan for the corresponding dataset. For the SOS data, the GIM_3g dataset exhibits the greatest contribution, followed by similar contributions from the GIM_4g and VIP datasets; the MCD12Q2 dataset has the smallest contribution. The MCD12Q2 dataset has a greater contribution in high-latitude areas near the Arctic Circle, but makes a smaller contribution in most other regions. The VIP dataset generally has a greater contribution than that of the MCD12Q2 dataset, with values ranging between 0 and 0.5 in 90% of areas. The overall contribution of the GIM_3g dataset is reasonably uniform, averaging at approximately 0.37. For the EOS data, the VIP dataset has the greatest contribution, followed by the GIM_4g dataset; the GIM_3g dataset has the smallest contribution. The contribution of the MCD12Q2 dataset remains relatively small, primarily distributed between 0 and 0.5. The VIP dataset has a positive correlation with latitude, with approximately 4.7% of areas of weights exceeding 0.8 in central Asia and parts of East Asia, whereas the contribution of the GIM_3g dataset remains lower across the entire region.
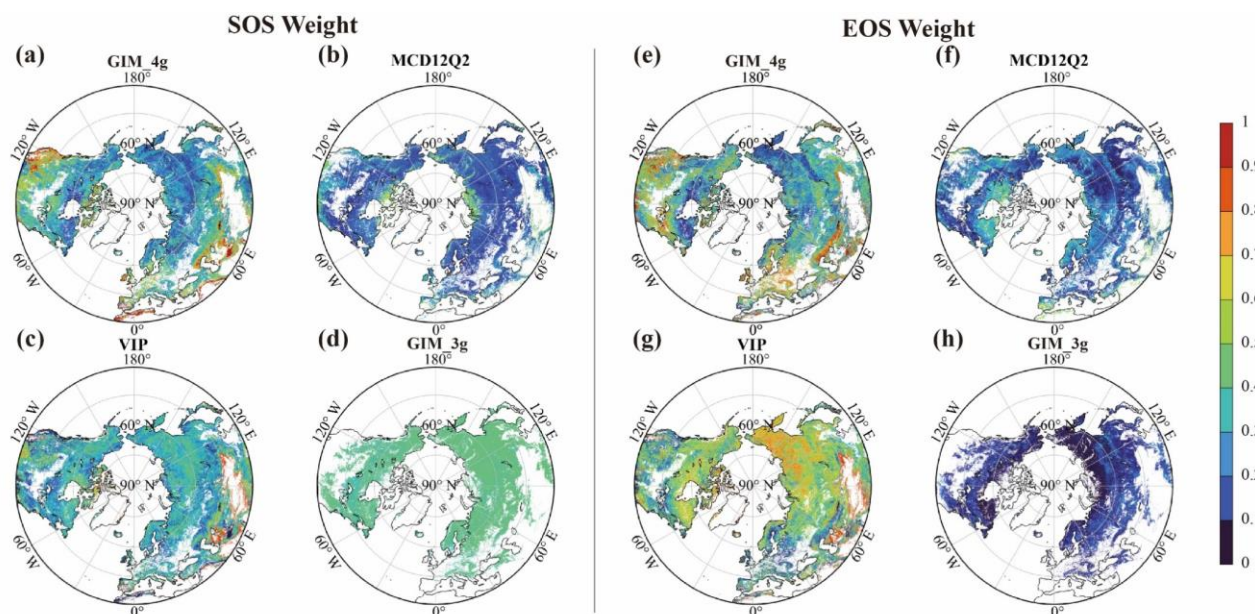
Figure 3: Spatial distribution of the mean contribution of the four datasets to the merged SOS and EOS results. (a–d) The mean SOS weight derived from the GIM_4g, MCD12Q2, VIP, and GIM_3g datasets, respectively, and (e–h) the mean EOS weight derived from the GIM_4g, MCD12Q2, VIP, and GIM_3g datasets, respectively.

3.3 Merged phenology dataset using the REA method

Figure 4 displays the merged mean SOS and EOS dates for the period 1982–2022. For the SOS, a general pattern of increase with latitude is evident, albeit with later occurrence of the SOS in southwestern North America, on the Qinghai–Tibet Plateau, etc. The highest proportion of the SOS falls within DOY 120–150 (40.0%), followed by DOY 90–120 (23.3%). The probabilities of the SOS within the intervals of DOY 60–90 and DOY 150–180 are comparable, i.e., 14.8% and 15.8%, respectively, with only 6.2% of areas experiencing the SOS later than DOY 180. The mean SOS obtained using the REA method is DOY 129 (std = 28 d). It demonstrates an overall increase in the EOS with latitude, with fewer trends observed in high-latitude areas above 60°N and eastern parts of North America. The distribution of the EOS appears more uniform after merging. Unlike the SOS data, the EOS primarily occurs within DOY 270–330 (93.1%). The mean EOS is DOY 283 (std = 23 d). Interannual variability in most regions for both the SOS and the EOS data is minimal; however, notable variations are observed in areas such as southwestern North America, Spain, Portugal, North Africa, West Asia, and Mongolia, consistent with the earlier analysis of data sources.

The mean uncertainty range (by Equation 6) of merged SOS and EOS dates and its coefficient of variation (CV) using the REA method during 1982-2022 are presented in Figure 4. The mean uncertainty range of SOS (EOS) dates is below 10d in more than 96% (94%) of regions, with less than 4% (5%) of regions exhibiting a mean uncertainty range exceeding 10d or 15d Fig. 4(b, e). The mean uncertainty range of SOS dates shows a negative correlation with latitude, whereas this trend is not evident in EOS dates. In Fig. 4(c, f), regarding the coefficient of variation (CV) in the uncertainty range of SOS (EOS) dates

from 1982 to 2022, more than 56% (73%) of regions have a CV below 1, 31% (18%) regions have a CV between 1 and 1.5, and only 13% (8%) of regions have a CV higher than 1.5. Regions with a CV below 1 in the uncertainty range of SOS and EOS dates are mostly located in the middle latitudes, but no observable correlation between CV and latitude changes is evident.
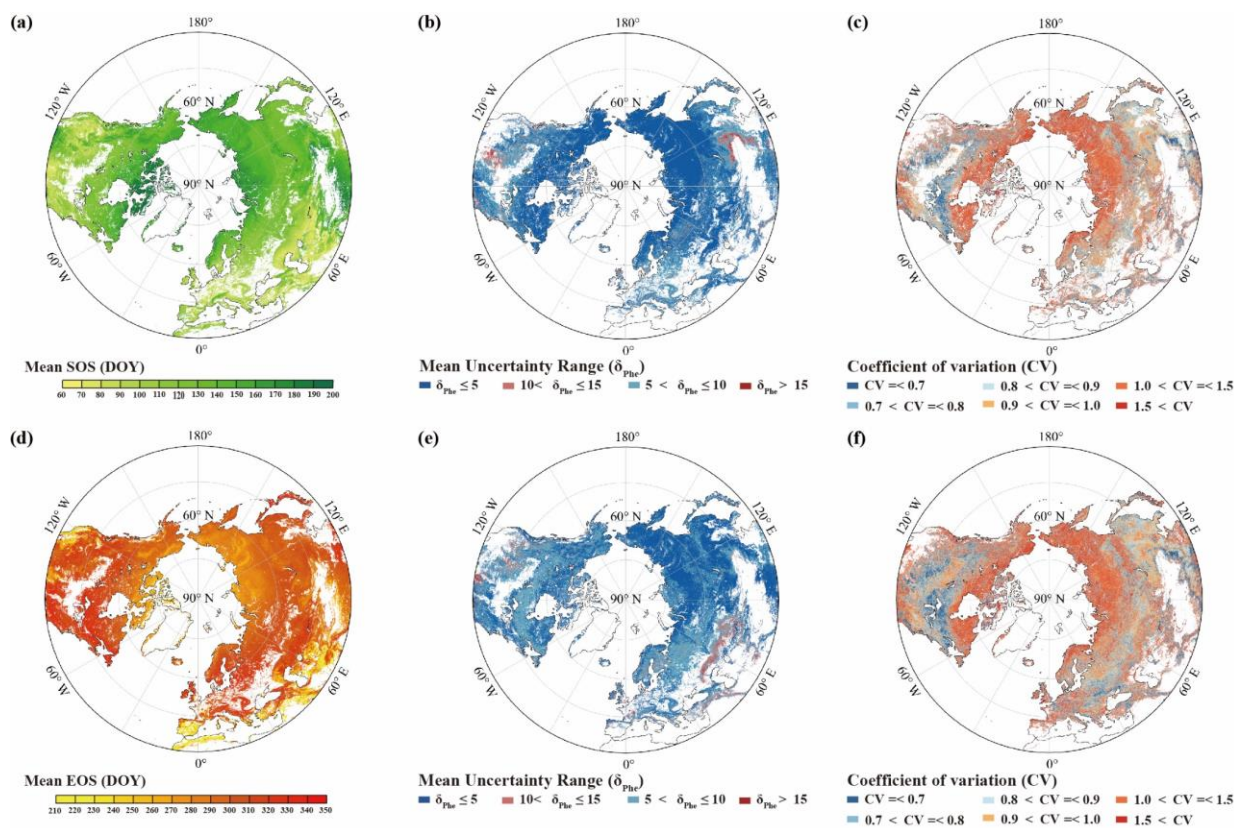
Figure 4: Merged mean (a) SOS and (b) EOS dates (DOY) obtained using the REA method for the period 1982–2022 and the uncertainty in the REA merged data. Mean uncertainty (δ_{Phe}) of SOS dates (b) and EOS (e) obtained using the REA method for the period 1982–2022, and its coefficient of variation (CV) in merged SOS (c) and EOS dates (f).

The PhenoCam dataset was used to evaluate each of the four vegetation datasets and the merged dataset. Verification results of the SOS and EOS data indicate that the merged data produced using the REA method has the best performance (Fig. 5). Specifically, the RMSE for the SOS and the EOS is 12 and 17 d, respectively. The correlation between the SOS and PhenoCam results is notably high at 0.84; for the EOS, it is 0.71. Evaluation of the four satellite-based SOS products shows that the GIM_3g dataset has the highest correlation coefficient and the lowest RMSE among the four datasets. However, it has more missing values spatially and a shorter time span, leading to fewer points for verification. The MCD12Q2 dataset has a correlation coefficient of 0.65 and an RMSE of 20 d, but its wider spatial coverage provides more points for verification. The GIM_4g dataset has a lower correlation with the PhenoCam dataset owing to outliers, resulting in an RMSE of 29 d. Compared with the PhenoCam dataset, the VIP dataset has a lower estimation in the SOS range of DOY 100–140, leading to a larger RMSE. The REA-based SOS dataset outperforms in terms of all indicators, with the lowest RMSE, UbRMSE, and standard

285 deviation, together with the highest correlation and lowest absolute bias, thereby demonstrating high consistency with the PhenoCam dataset.

In the evaluation of the EOS, the MCD12Q2 dataset has the best results among the four datasets, and except for the REA result, it has the highest correlation coefficient and the lowest RMSE. The GIM_4g dataset shows good performance but tends to overestimate the EOS, resulting in an RMSE of 43 d. Both the VIP and the GIM_3g datasets overestimate the EOS owing

290 to their spatial and temporal distributions, with RMSEs of 46 and 35 d, respectively. It is evident from Fig. 5 that the REA dataset demonstrates the highest accuracy and best consistency with the PhenoCam dataset, outperforming the four other datasets in terms of all indicators, with the lowest RMSE, UbRMSE, and standard deviation, together with the highest correlation and lowest absolute bias.
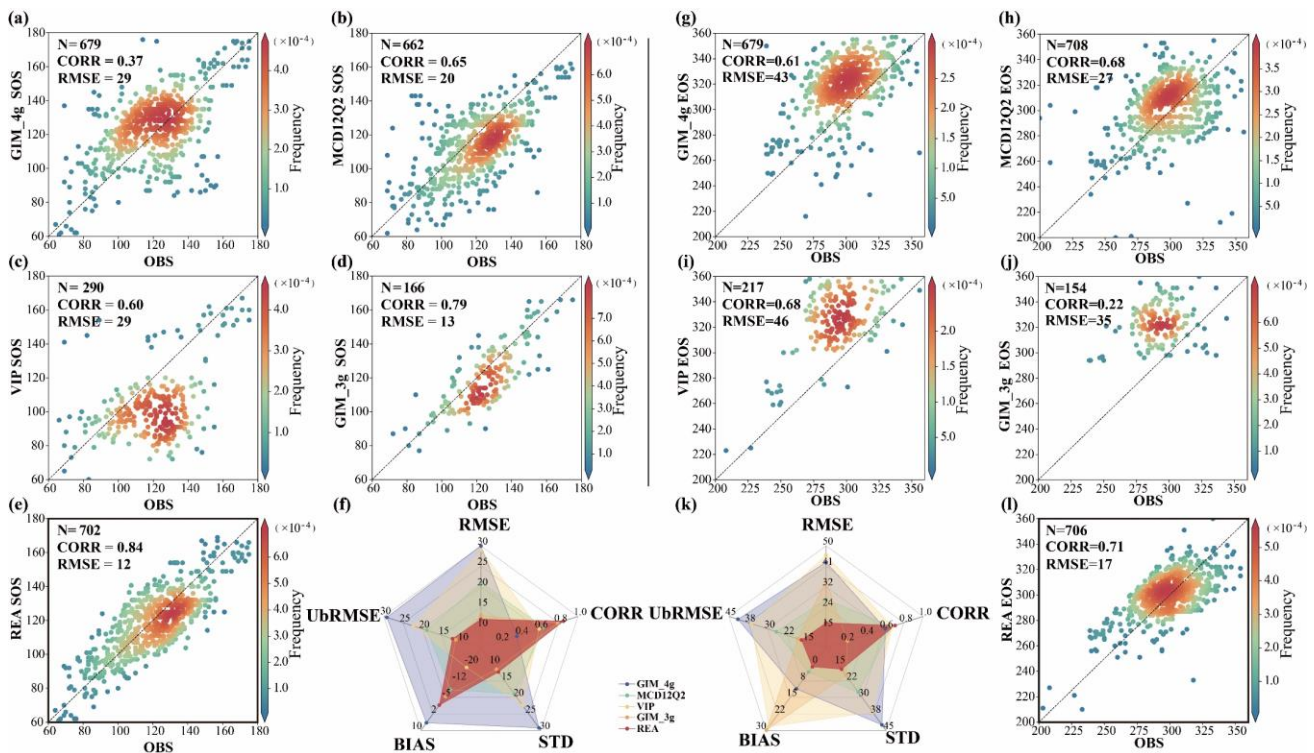
Figure 5: Scatterplots and radar charts of performance for each phenology dataset and the merged phenology dataset obtained using
295 **the REA method. (**a–e) SOS evaluation results of the GIM_4g, MCD12Q2, VIP, GIM_3g, and REA datasets, respectively, (f) radar chart
of the SOS evaluation results, (g–j and l) EOS evaluation results of the GIM_4g, MCD12Q2, VIP, GIM_3g, and REA datasets, respectively,
and (k) radar chart of the EOS evaluation results. OBS indicates ground-based PhenoCam phenological dates, RMSE indicates the root mean
square error, UbRMSE indicates the unbiased RMSE, BIAS indicates the mean difference between the satellite-based results and the ground-
300 based verification results, and STD indicates the standard deviation.

Due to differences in time scales between PhenoCam data and different phenology datasets, we selected a long-term PhenoCam site that aligns with the time span of these phenology datasets to evaluate the merged dataset. We have chosen an American PhenoCam site characterized by deciduous broad-leaved forest and the time range is 2002-2010 for SOS and 2001-2009 for EOS. As shown in the time series plot in Figure 6, the consistency between the REA and PhenoCam data for both

305 SOS and EOS compared to other datasets is the largest. Additionally, most vegetation phenology products demonstrate higher consistency with PhenoCam data for SOS compared to EOS.
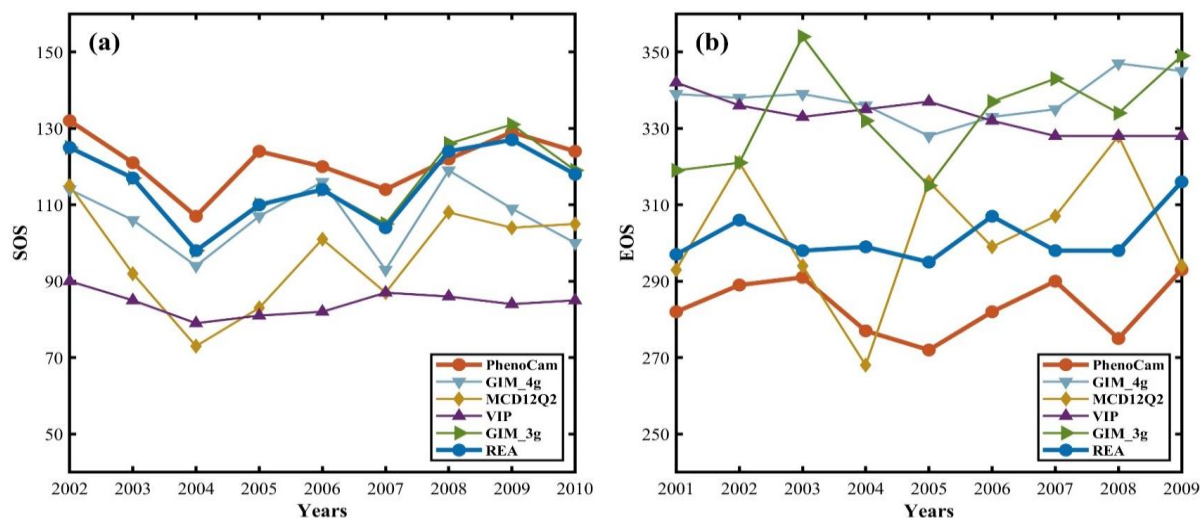
Figure 6: Time series of a PhenoCam site data with each phenology dataset and the merged phenology dataset obtained using the REA method. (a) SOS time series of the PhenoCam, GIM_4g, MCD12Q2, VIP, GIM_3g, and REA datasets, respectively, (b) EOS time series of the PhenoCam, GIM_4g, MCD12Q2, VIP, GIM_3g, and REA datasets, respectively.

3.4 Temporal trends of phenology based on the merged dataset

It is evident from Fig. 7(a) that the SOS exhibits a significant ($p < 0.01$) trend of advance over the period 1982–2022, with a rate of advance of approximately 0.24 d yr^{-1}. Figure 7(b) presents the spatial distribution of the SOS trends obtained using the Mann–Kendall test. Approximately 65.58% of regions exhibit a trend of advance, with 46.25% of regions exhibiting 315 a significant ($p < 0.05$) trend.

Figure 7(c) illustrates that the EOS exhibits a significant trend of delay with a rate of 0.16 d yr^{-1} ($p < 0.01$). It is evident from Fig. 7(d) that the proportion of areas experiencing delayed EOS in regions above 30°N is 66.08% (comprising 43.21% significant at $p < 0.05$), consistent with the corresponding trend depicted in Fig. 7(c). Apart from southwestern to northeastern regions of North America, Europe, the Middle East, and certain high-latitude areas in Asia, EOS delay is predominant. Over 320 the study area, 45.69% of regions exhibit SOS advance and EOS delay, 18.97% show SOS advance and EOS advance, 19.49% demonstrate SOS delay and EOS delay, and 14.42% show SOS delay and EOS advance.
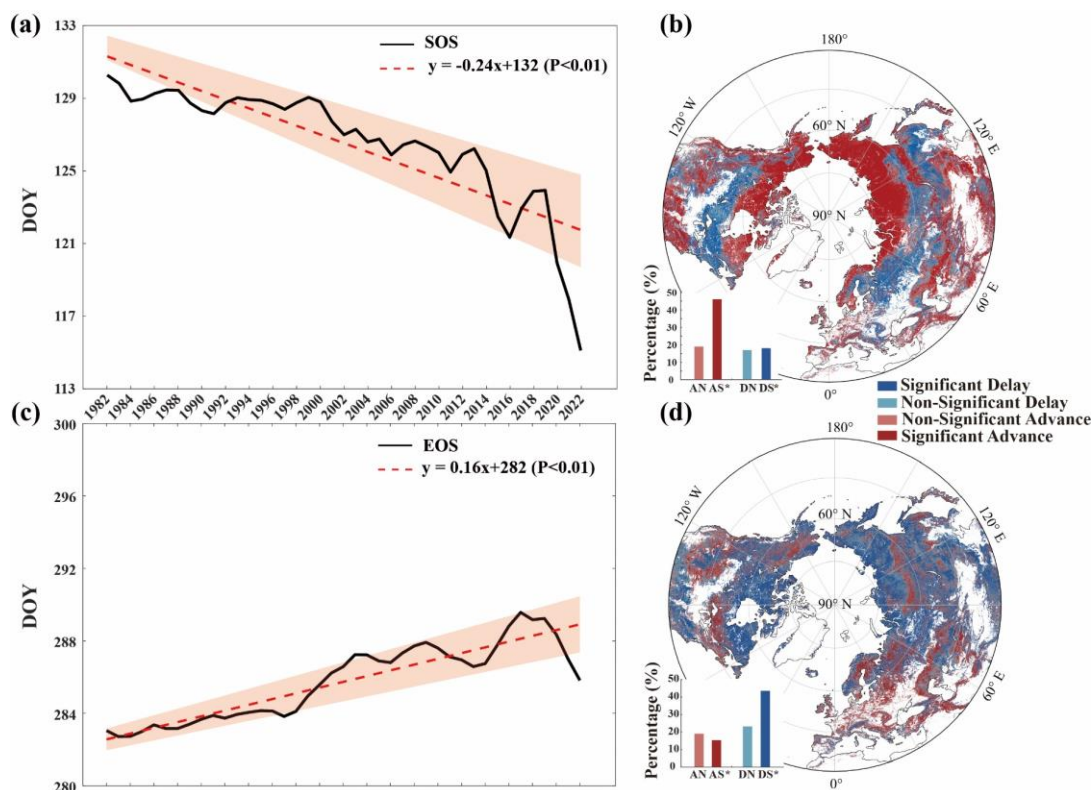
Figure 7: Temporal and spatial trends of the SOS and the EOS over the period 1982–2022 based on the merged dataset obtained using the REA method. (a) Temporal trend of the SOS over the period 1982-2022, (b) Spatial trend of the SOS over the period 1982-2022, (c)Temporal trend of the EOS over the period 1982-2022, (d) Spatial trend of the EOS over the period 1982-2022. The shaded area in (a) and (c) indicates uncertainty at one standard deviation.

4 Discussion and Conclusions

Different vegetation phenology datasets have been produced and were widely used, but we found that differences of more than two months (>60 d) exist in key phenological dates among these datasets, consistent with previous reports (Zhang et al., 2020). The substantial differences among the various vegetation phenology datasets are related mainly to differences in spatial and temporal resolutions, extraction methods, spectral response functions, and the complexity of surface backgrounds (Trishchenko et al., 2002; Zhang et al., 2020). For example, phenology datasets with low spatial resolution experience the problem of the mixed-pixel effect (Chen et al., 2018), which can result in large differences in phenological dates compared with those derived using high-resolution phenology datasets. Thus, a merged phenology dataset is required to exploit the advantages of the various phenology datasets available.

Data fusion methods generally include unmixing-based, weight-function-based, and Bayesian-based methods (Gevaert and García-Haro, 2015; Piao et al., 2019). In the field of vegetation phenology, fusion methods based on raw remote sensing data, such as the Spatial and Temporal Adaptive Reflectance Fusion Model (Gao et al., 2006) and the Enhanced Spatial and

340 Temporal Adaptive Reflectance Fusion Model (Zhu et al., 2010), are generally influenced by complex vegetation types, vegetation growth status, and the process of coefficient determination (Sisheber et al., 2022). The reflectance of vegetation endmembers changes nonlinearly, and likely results in poor performance in vegetation phenology extraction. The REA method is not based on the hypothesis that pixel reflectance changes linearly; instead, it merges annual phenology products directly based on their reliability. Compared with commonly used data fusion methods, the REA method offers advantages in terms of

345 simplicity and efficiency(Lu et al., 2021), and it considers the reliability of the data, which contrasts with traditional methods that simply calculate the mean value of various data. The simple averaging method treats each data source equally, even though the uncertainties of each dataset are likely to vary across time and space(Lu et al., 2021; Wang et al., 2019), introducing inaccuracy to the merged dataset. The REA method considers the temporal correlation of vegetation phenology data by employing a voting principle (Giorgi and Mearns, 2002), and this approach facilitates convergence of data while retaining

350 differences in terms of the spatial distribution, thereby offering advantages with respect to multisource data fusion.

   Compared with individual vegetation phenology datasets, i.e., the MCD12Q2, VIP, GIM_3g, and GIM_4g datasets, our REA-based phenology dataset has a long-term sequence spanning 1982–2022 with a spatial resolution of 0.05°. The REA method facilitates better convergence and produces a unified phenology product with high reliability. To verify the reliability of the merged data product, we compared it against the ground-based PhenoCam dataset. Results revealed that the REA-based

355 SOS and EOS exhibit the lowest RMSE and the highest correlation coefficients compared with those of the other four datasets, suggesting that the REA method offers high processing efficiency and accuracy. Global climate change has notably altered the timing of vegetation phenology events, including the advance of the SOS (Piao et al., 2019) and the delay of the EOS. Based on the merged phenology dataset, our results were consistent with those earlier findings, i.e., over the long-term period of 1982–2022, advance (delay) in the SOS (EOS) has occurred at the rate of 0.24 (0.16) d yr^{-1}. Shifts in vegetation phenology

360 affect ecosystem structure (Kharouba et al., 2018; Yang and Rudolf, 2010), consequentially affecting biodiversity (Renner and Zohner, 2018), terrestrial carbon and water cycles (Piao et al., 2020), and the climate system (Green et al., 2017; Piao et al., 2020). The establishment of a comprehensive and reliable vegetation phenology dataset is therefore profoundly important. Our study demonstrates that an invaluable vegetation phenology dataset can be obtained by applying the REA method, and that this dataset could be used for subsequent analyses, such as examining vegetation phenology dynamics and their impacts on the

365 terrestrial carbon cycle and water balance, and providing climatic feedback for global vegetation dynamics modeling.

Data availability

The MCD12Q2 phenology dataset is available at https://lpdaac.usgs.gov/products/mcd12q2v061/(Friedl et al., 2022), the VIP phenology dataset is available at https://lpdaac.usgs.gov/products/vipphen_ndviv004/ (Didan and Barreto, 2016), the GIM_3g phenology dataset is available at http://data.globalecology.unh.edu/data/GIMMS_NDVI3g_Phenology/ (Wang et al., 2019),

370 the GIM_4g phenology dataset is available at https://doi.org/10.5281/zenodo.11136967 (Chen and Fu, 2024), the camera-based phenology dataset is available at https://daac.ornl.gov/, http://www.sizenken.biodic.go.jp/, and http://www.pheno-eye.org/, the

land use dataset is available at https://lpdaac.usgs.gov/products/mcd12q1v061/ (Friedl and Sulla-Menashe, 2022), and the REA phenology dataset is available at https://doi.org/10.5281/zenodo.11127281 (Cui and Fu, 2024).

Competing interests

375   The contact author declares that none of the authors has any competing interests.

Author contribution

YHF developed the preliminary conceptualization; YC performed the study, YC, YHF and YZ wrote the manuscript; YHF and YZ supervised the manuscript construction and revision; SC, YG, ML, ZJ participated in reviewing and editing the paper. All authors have read and approved the paper.

380   **Acknowledgments**

The work was supported by the National Funds for Distinguished Young Youths (Grant No. 42025101), the National Key Research and Development Program of China (Grant No. 2023YFF0805604), the Fundamental Research Funds for the Central Universities (2243300004), and the 111 Project (Grant No. B18006). We thank Liwen Bianji for editing the English text of a draft of this manuscript.

385   **References**

Badeck, F.-W., Bondeau, A., Böttcher, K., Doktor, D., Lucht, W., Schaber, J., and Sitch, S.: Responses of spring phenology to climate change, New Phytologist, 162, 295–309, https://doi.org/10.1111/j.1469-8137.2004.01059.x, 2004.

Chen, S. and Fu, Y.: Vegetation phenology data based on GIMMS4g NDVI from 1982 to 2020 [data set], https://doi.org/10.5281/zenodo.11136967, 2024.

390   Chen, S., Fu, Y. H., Li, M., Jia, Z., Cui, Y., and Tang, J.: A new temperature–photoperiod coupled phenology module in LPJ-GUESS model v4. 1: optimizing estimation of terrestrial carbon and water processes [data set], Geoscientific Model Development, 17, 2509–2523, https://doi.org/10.5194/gmd-17-2509-2024, 2024.

Chen, X., Wang, D., Chen, J., Wang, C., and Shen, M.: The mixed pixel effect in land surface phenology: A simulation study, Remote Sensing of Environment, 211, 338–344, https://doi.org/10.1016/j.rse.2018.04.030, 2018.

395   Cui, Y. and Fu, Y.: A vegetation phenology dataset by integrating multiple sources using the Reliability Ensemble Averaging method [data set], https://doi.org/10.5281/zenodo.11127281, 2024.

Delbart, N., Beaubien, E., Kergoat, L., and Le Toan, T.: Comparing land surface phenology with leafing and flowering observations from the PlantWatch citizen network, Remote Sensing of Environment, 160, 273–280,

https://doi.org/10.1016/j.rse.2015.01.012, 2015.

400 Didan, K. and Barreto, A.: NASA MEaSUREs Vegetation Index and Phenology (VIP) Phenology NDVI Yearly Global 0.05Deg CMG [data set], https://doi.org/10.5067/MEaSUREs/VIP/VIPPHEN_NDVI.004, 2016.

Didan, K., Barreto-Munoz, A., Miura, T., Tsend-Ayush, J., Zhang, X., Friedl, M., and Meyer, D.: Multi-Sensor Vegetation Index and Phenology Earth Science Data Records, 2018.

Ettinger, A. K., Chamberlain, C. J., Morales-Castilla, I., Buonaiuto, D. M., Flynn, D. F. B., Savas, T., Samaha, J. A., and

405 Wolkovich, E. M.: Winter temperatures predominate in spring phenological responses to warming, Nature Climate Change, 10, 1137–1142, https://doi.org/10.1038/s41558-020-00917-3, 2020.

Fensholt, R. and Proud, S. R.: Evaluation of Earth Observation based global long term vegetation trends—Comparing GIMMS and MODIS global NDVI time series, Remote sensing of Environment, 119, 131–147, https://doi.org/10.1016/j.rse.2011.12.015, 2012.

410 Friedl, M. and Sulla-Menashe, D.: MODIS/Terra+Aqua Land Cover Type Yearly L3 Global 500m SIN Grid V061 [data set], https://doi.org/10.5067/MODIS/MCD12Q1.061, 2022.

Friedl, M., Gray, J., and Sulla-Menashe, D.: MODIS/Terra+Aqua Land Cover Dynamics Yearly L3 Global 500m SIN Grid V061 [data set], https://doi.org/10.5067/MODIS/MCD12Q2.061, 2022.

Fu, Y. H., Piao, S., Op de Beeck, M., Cong, N., Zhao, H., Zhang, Y., Menzel, A., and Janssens, I. A.: Recent spring phenology

415 shifts in western C entral E urope based on multiscale observations, Global ecology and biogeography, 23, 1255–1263, https://doi.org/10.1111/geb.12210, 2014.

Fu, Y. H., Geng, X., Chen, S., Wu, H., Hao, F., Zhang, X., Wu, Z., Zhang, J., Tang, J., and Vitasse, Y.: Global warming is increasing the discrepancy between green (actual) and thermal (potential) seasons of temperate trees, Global Change Biology, 29, 1377–1389, https://doi.org/10.1111/gcb.16545, 2023.

420 Gao, F., Masek, J., Schwaller, M., and Hall, F.: On the blending of the Landsat and MODIS surface reflectance: Predicting daily Landsat surface reflectance, IEEE Transactions on Geoscience and Remote sensing, 44, 2207–2218, https://doi.org/10.1109/TGRS.2006.872081, 2006.

Geng, X., Fu, Y. H., Hao, F., Zhou, X., Zhang, X., Yin, G., Vitasse, Y., Piao, S., Niu, K., and De Boeck, H. J.: Climate warming increases spring phenological differences among temperate trees, Global Change Biology, 26, 5979–5987,

425 https://doi.org/10.1111/gcb.15301, 2020.

Gevaert, C. M. and García-Haro, F. J.: A comparison of STARFM and an unmixing-based algorithm for Landsat and MODIS data fusion, Remote sensing of Environment, 156, 34–44, https://doi.org/10.1016/j.rse.2014.09.012, 2015.

Giorgi, F. and Mearns, L. O.: Calculation of Average, Uncertainty Range, and Reliability of Regional Climate Changes from AOGCM Simulations via the "Reliability Ensemble Averaging" (REA) Method, Journal of Climate, 15, 1141–1158,

430 https://doi.org/10.1175/1520-0442(2002)015<1141:COAURA>2.0.CO;2, 2002.

Gray, J., Sulla-Menashe, D., and Friedl, M. A.: User guide to collection 6 modis land cover dynamics (mcd12q2) product, NASA EOSDIS Land Processes DAAC: Missoula, MT, USA, 6, 1–8, 2019.

Green, J. K., Konings, A. G., Alemohammad, S. H., Berry, J., Entekhabi, D., Kolassa, J., Lee, J.-E., and Gentine, P.: Regionally strong feedbacks between the atmosphere and terrestrial biosphere, Nature geoscience, 10, 410–414, https://doi.org/10.1038/ngeo2957, 2017.

Kendall, M. G.: Rank correlation methods. 2nd impression, Charles Griffin and Company Ltd. London and High Wycombe, 1975.

Kharouba, H. M., Ehrlén, J., Gelman, A., Bolmgren, K., Allen, J. M., Travers, S. E., and Wolkovich, E. M.: Global shifts in the phenological synchrony of species interactions over recent decades, Proceedings of the National Academy of Sciences, 115, 5211–5216, https://doi.org/10.1073/pnas.1714511115, 2018.

Liu, Q., Fu, Y. H., Zhu, Z., Liu, Y., Liu, Z., Huang, M., Janssens, I. A., and Piao, S.: Delayed autumn phenology in the Northern Hemisphere is related to change in both climate and spring phenology, Global change biology, 22, 3702–3711, 2016.

Lu, J., Wang, G., Chen, T., Li, S., Hagan, D. F. T., Kattel, G., Peng, J., Jiang, T., and Su, B.: A harmonized global land evaporation dataset from model-based products covering 1980–2017, Earth System Science Data, 13, 5879–5898, https://doi.org/10.5194/essd-13-5879-2021, 2021.

Mao, P., Zhang, J., Li, M., Liu, Y., Wang, X., Yan, R., Shen, B., Zhang, X., Shen, J., and Zhu, X.: Spatial and temporal variations in fractional vegetation cover and its driving factors in the Hulun Lake region, Ecological Indicators, 135, 108490, https://doi.org/10.1016/j.ecolind.2021.108490, 2022.

Moon, M., Richardson, A. D., and Friedl, M. A.: Multiscale assessment of land surface phenology from harmonized Landsat 8 and Sentinel-2, PlanetScope, and PhenoCam imagery, Remote Sensing of Environment, 266, 112716, https://doi.org/10.1016/j.rse.2021.112716, 2021.

Peng, D., Zhang, X., Wu, C., Huang, W., Gonsamo, A., Huete, A. R., Didan, K., Tan, B., Liu, X., and Zhang, B.: Intercomparison and evaluation of spring phenology products using National Phenology Network and AmeriFlux observations in the contiguous United States, Agricultural and Forest Meteorology, 242, 33–46, https://doi.org/10.1016/j.agrformet.2017.04.009, 2017.

Peñuelas, J., Rutishauser, T., and Filella, I.: Phenology feedbacks on climate change, Science, 324, 887–888, https://doi.org/10.1126/science.1173004, 2009.

Piao, S., Fang, J., Zhou, L., Ciais, P., and Zhu, B.: Variations in satellite-derived phenology in China's temperate vegetation, Global change biology, 12, 672–685, https://doi.org/10.1111/j.1365-2486.2006.01123.x, 2006.

Piao, S., Fang, J., Ciais, P., Peylin, P., Huang, Y., Sitch, S., and Wang, T.: The carbon balance of terrestrial ecosystems in China, Nature, 458, 1009–1013, https://doi.org/10.1038/nature07944, 2009.

Piao, S., Liu, Q., Chen, A., Janssens, I. A., Fu, Y., Dai, J., Liu, L., Lian, X. U., Shen, M., and Zhu, X.: Plant phenology and global climate change: Current progresses and challenges, Global change biology, 25, 1922–1940, https://doi.org/10.1111/gcb.14619, 2019.

Piao, S., Wang, X., Park, T., Chen, C., Lian, X. U., He, Y., Bjerke, J. W., Chen, A., Ciais, P., and Tømmervik, H.: Characteristics, drivers and feedbacks of global greening, Nature Reviews Earth & Environment, 1, 14–27, https://doi.org/10.1038/s43017-

019-0001-x, 2020.

Renner, S. S. and Zohner, C. M.: Climate change and phenological mismatch in trophic interactions among plants, insects, and vertebrates, Annual review of ecology, evolution, and systematics, 49, 165–182, https://doi.org/10.1146/annurev-ecolsys-470   110617-062535, 2018.

Richardson, A. D., Anderson, R. S., Arain, M. A., Barr, A. G., Bohrer, G., Chen, G., Chen, J. M., Ciais, P., Davis, K. J., and Desai, A. R.: Terrestrial biosphere models need better representation of vegetation phenology: results from the North American Carbon Program Site Synthesis, Global Change Biology, 18, 566–584, https://doi.org/10.1111/j.1365-2486.2011.02562.x, 2012.

475   Ruan, Y., Ruan, B., Xin, Q., Liao, X., Jing, F., and Zhang, X.: phenoC++: An open-source tool for retrieving vegetation phenology from satellite remote sensing data, Frontiers in Environmental Science, 11, 215, https://doi.org/10.3389/fenvs.2023.1097249, 2023.

Sisheber, B., Marshall, M., Mengistu, D., and Nelson, A.: Tracking crop phenology in a highly dynamic landscape with knowledge-based Landsat–MODIS data fusion, International journal of applied earth observation and geoinformation, 106, 480   102670, https://doi.org/10.1016/j.jag.2021.102670, 2022.

Sparks, T. H. and Carey, P. D.: The responses of species to climate over two centuries: an analysis of the Marsham phenological record, 1736-1947, Journal of Ecology, 321–329, https://doi.org/10.2307/2261570, 1995.

Sulla-Menashe, D. and Friedl, M. A.: User guide to collection 6 MODIS land cover (MCD12Q1 and MCD12C1) product, Usgs: Reston, Va, Usa, 1, 18, 2018.

485   Sun, J., Wang, X., Cao, Y., Li, H., and Jung, K.: Analysis of spatial and temporal evolution of hydrological and meteorological elements in Nenjiang River basin, China, Theoretical and applied climatology, 137, 941–961, https://doi.org/10.1007/s00704-018-2641-z, 2019.

Tang, J., Körner, C., Muraoka, H., Piao, S., Shen, M., Thackeray, S. J., and Yang, X.: Emerging opportunities and challenges in phenology: a review, Ecosphere, 7, e01436, https://doi.org/10.1002/ecs2.1436, 2016.

490   Trishchenko, A. P., Cihlar, J., and Li, Z.: Effects of spectral response function on surface reflectance and NDVI measured with moderate resolution satellite sensors, Remote Sensing of Environment, 81, 1–18, https://doi.org/10.1016/S0034-4257(01)00328-5, 2002.

Walker, J. J., De Beurs, K. M., Wynne, R. H., and Gao, F.: Evaluation of Landsat and MODIS data fusion products for analysis of dryland forest phenology, Remote Sensing of Environment, 117, 381–393, 2012.

495   Wang, X., Xiao, J., Li, X., Cheng, G., Ma, M., Zhu, G., Altaf Arain, M., Andrew Black, T., and Jassal, R. S.: No trends in spring and autumn phenology during the global warming hiatus, Nat Commun, 10, 2389, https://doi.org/10.1038/s41467-019-10235-8, 2019.

Xu, Y., Gao, X., and Giorgi, F.: Upgrades to the reliability ensemble averaging method for producing probabilistic climate-change projections, Climate Research, 41, 61–81, https://doi.org/10.3354/cr00835, 2010.

500   Yang, L. H. and Rudolf, V. H. W.: Phenology, ontogeny and the effects of climate change on the timing of species interactions,

Ecology letters, 13, 1–10, https://doi.org/10.1111/j.1461-0248.2009.01402.x, 2010.

Zhang, H., Chuine, I., Regnier, P., Ciais, P., and Yuan, W.: Deciphering the multiple effects of climate warming on the temporal shift of leaf unfolding, Nature Climate Change, 12, 193–199, https://doi.org/10.1038/s41558-021-01261-w, 2022.

Zhang, J., Zhao, J., Wang, Y., Zhang, H., Zhang, Z., and Guo, X.: Comparison of land surface phenology in the Northern Hemisphere based on AVHRR GIMMS3g and MODIS datasets, ISPRS Journal of Photogrammetry and Remote Sensing, 169, 1–16, 2020.

Zhou, X., Geng, X., Yin, G., Hänninen, H., Hao, F., Zhang, X., and Fu, Y. H.: Legacy effect of spring phenology on vegetation growth in temperate China, Agricultural and Forest Meteorology, 281, 107845, https://doi.org/10.1016/j.agrformet.2019.107845, 2020.

Zhou, Y.: Understanding urban plant phenology for sustainable cities and planet, Nature Climate Change, 12, 302–304, https://doi.org/10.1038/s41558-022-01331-7, 2022.

Zhou, Y. and Liu, J.: Spatio-temporal Analysis of Vegetation Phenology with Multiple Methods over the Tibetan Plateau based on MODIS NDVI Data, Remote Sensing Technology and Application, 33, 486–498, https://doi.org/10.11873/j.issn.1004-0323.2018.3.0486, 2018.

Zhu, X., Chen, J., Gao, F., Chen, X., and Masek, J. G.: An enhanced spatial and temporal adaptive reflectance fusion model for complex heterogeneous regions, Remote Sensing of Environment, 114, 2610–2623, https://doi.org/10.1016/j.rse.2010.05.032, 2010.

505

510

515